nature communications

Article

https://doi.org/10.1038/s41467-024-53871-5

High-density asymmetric iron dual-atom sites for efficient and stable electrochemical water oxidation

Received: 6 May 2024

Accepted: 24 October 2024

Published online: 01 November 2024

Check for updates

Lili Zhang[1,7], Ning Zhang[2,7], Huishan Shang[1] ✉, Zhiyi Sun[3], Zihao Wei[3], Jingtao Wang[1] ✉, Yuanting Lei[1], Xiaochen Wang[1], Dan Wang[1], Yafei Zhao[1], Zhongti Sun[4] ✉, Fang Zhang[5], Xu Xiang[6], Bing Zhang[1] & Wenxing Chen[3] ✉

Double-atom catalysts (DACs) have opened distinctive paradigms in the field of rapidly developing atomic catalysis owing to their great potential for promoting catalytic performance in various reaction systems. However, increasing the loading and extending the service life of metal active centres represents a considerable challenge for the efficient utilization of DACs. Here, we rationally design asymmetric nitrogen, sulfur-coordinated diatomic iron centres on highly defective nitrogen-doped carbon nanosheets (denoted *A*-$Fe_2S_1N_5$/SNC, *A*: asymmetric), which possess the atomic configuration of the N_2S_1Fe-FeN_3 moiety. The abundant defects and low-electronegativity heteroatoms in the carbon-based framework endow *A*-$Fe_2S_1N_5$/SNC with a high loading of 6.72 wt%. Furthermore, *A*-$Fe_2S_1N_5$/SNC has a low overpotential of 193 mV for the oxygen evolution reaction (OER) at 10 mA cm^{-2}, outperforming commercial RuO_2 catalysts. In addition, *A*-$Fe_2S_1N_5$/SNC exhibits extraordinary stability, maintaining > 97% activity for over 2000 hours during the OER process. This work provides a practical scheme for simultaneously balancing the activity and stability of DACs towards electrocatalysis applications.

Electrocatalytic water splitting and metal–air batteries are considered promising options in sustainable energy conversion technologies. As the proton and electron provider on the anode electrode, the oxygen evolution reaction (OER) plays an important role in these devices. However, the four-electron OER process involves O–H bond rupture and O–O bond formation, the kinetics of which are sluggish; this is necessary for the development of highly efficient OER catalysts. To date, iridium- and ruthenium-based catalysts are still the benchmark commercial OER catalysts; however, their low crustal abundance, high cost, and inferior durability limit their long-term development[1–3]. Consequently, developing earth-abundant and high-intrinsic-activity OER catalysts is important for improving current energy technology.

Recently, single-atom catalysts (SACs) with diverse well-defined coordination configurations have attracted increasing attention due to their maximized atomic utilization and high catalytic activity[4,5]. Among the SACs developed in recent years, metal–N–C catalysts with symmetric metal–N_4 coordination structures have been extensively studied[6]. However, their OER performance is still unsatisfactory compared with that of benchmark iridium- and ruthenium-based catalysts due to their symmetric electron distribution. To overcome this challenge, it is necessary to adjust the local coordination environment

[1]School of Chemical Engineering, Zhengzhou University, Zhengzhou 450001, P. R. China. [2]Changchun Institute of Applied Chemistry Chinese Academy of Sciences, Changchun, P. R. China. [3]Energy & Catalysis Center, School of Materials Science and Engineering, Beijing Institute of Technology, Beijing 100081, P. R. China. [4]School of Materials Science and Engineering, Jiangsu University, Zhen-Jiang, Jiangsu 212013, P. R. China. [5]Analysis and Testing Center, Beijing Institute of Technology, Beijing 100081, P. R. China. [6]State Key Laboratory of Chemical Resource Engineering, Beijing University of Chemical Technology, Beijing 100029, P. R. China. [7]These authors contributed equally: Lili Zhang, Ning Zhang. ✉e-mail: shanghs@zzu.edu.cn; jingtaowang@zzu.edu.cn; ztsun@ujs.edu.cn; wxchen@bit.edu.cn

around metal–N_4 SACs properly. The adsorption strength of OER intermediates can be optimized by breaking the inherent symmetric charge distribution[7]. In addition, SACs contain unitary active centers, resulting in the binding of only one oxygen-containing OER intermediate (e.g., O*, OH*, OOH*), which limits their high OER activity[8]. With the expansion of SACs, double-atom catalysts (DACs) have emerged as ideal candidates for highly efficient OER. The inherent advantages of SACs and the newly identified emerging binding sites/modes that occur within the catalytic centers for DACs are promising for overcoming the inherent activity limits[9]. The heterogeneous nature of the coordination configuration may lead to the formation of distinct catalytically active sites and reaction pathways, which in turn can influence the overall catalytic performance. Moreover, the atomic spatial configuration, the surrounding chelating atoms, and the coordination number are of paramount importance in optimizing the coordination environment of DACs[10]. Accordingly, dual-metal sites can be classified into three categories based on their coordination environment: binuclear homologous dual-metal sites, binuclear heterologous dual-metal sites, and isolated dual-metal sites[11]. Among these, the symmetric distribution of M_2 sites on M_2–N–C DACs belongs to the binuclear homologous dual-metal site pairs[12]. These catalysts have higher metal loadings than the isolated metal site catalysts due to the preferred diatomic pairs at high metal loadings. The OER involves multiple proton-coupled electron-transfer processes, and the symmetric distribution of M_2–N–C DACs possesses unitary active sites, which makes it difficult to achieve the optimal adsorption state of multiple reaction intermediates[13]. Consequently, the asymmetrical charge distribution on homonuclear dual-metal sites can maximize the potential of DACs for multistep reactions, which makes the optimization of activity and selectivity feasible.

Iron (Fe), which is a congener of Ru for the first transition series, is considered a promising OER catalyst because of its earth abundance, low cost, and biocompatibility[14,15]. It has been reported that the monomeric amidate-ligated Fe(III)-aqua complex can be used as an electrocatalyst for the OER with a Faradaic yield of 45%[16]. However, the mononuclear Fe-based complex may collapse during the OER due to hydrogen atom transfer at the active Fe sites, which leads to stability problems[17]. Interestingly, the binuclear Fe complex $[tpa(H_2O)FeOFe(H_2O)tpa](ClO_4)_4$ was constructed as an efficient OER catalyst, which was six times greater than that of the mononuclear $[Fe(OTf\ or\ Cl)_2(tpa)]$ complex[18]. Notably, the OER kinetics on Fe–N–C were sluggish because of the strong O* binding strength on the Fe sites[19]. Consequently, the rate-determining step for Fe–N–C towards the OER is the conversion of *O to *OOH. Inspired by the progress in OER research on Fe-based complexes and Fe–N–C, the construction of an asymmetric iron dual-atom catalyst is one of the most promising approaches for developing highly active and durable OER.

In this work, we design a sulfur, nitrogen-codoping carbonaceous support (SNC) with high defects to anchor Fe–Fe dual-atom sites (*A*-$Fe_2S_1N_5$/SNC) through a multilayer stabilization strategy involving defect capture and coordination riveting. Comprehensive characterization verified that the asymmetric diatomic FeS_1N_2–FeN_3 moieties were densely dispersed on the support, with a high metal mass loading of 6.72 wt%. The *A*-$Fe_2S_1N_5$/SNC catalyst displays high OER activity. In alkaline electrolytes, *A*-$Fe_2S_1N_5$/SNC has a low overpotential of 193 mV at 10 mA cm^{-2}. Under constant current, *A*-$Fe_2S_1N_5$/SNC can catalyze the OER for more than 2000 h, which results in extraordinary stability compared with other reported atomically dispersed electrocatalysts. The theoretical calculations indicate that the enhanced OER activity derived from spontaneous electric polarization occurred at the iron dual-atom sites of the asymmetric *A*-$Fe_2S_1N_5$/SNC catalyst. Moreover, the alkaline AEMWE (anion exchange membrane water electrolyzer) catalyzed by *A*-$Fe_2S_1N_5$/SNC displays good performance, indicating its broad practical application potential. In particular, other asymmetrically coordinated *A*-$M_2S_1N_5$/SNC catalysts (M = Co, Ni, Cu, and Mn) with high metal loading were also prepared and investigated, demonstrating the universality of the developed strategy.

Results

Synthesis and characterization of *A*-$Fe_2S_1N_5$/SNC

A continuous two-step pyrolysis and carbonization approach, as shown in Fig. 1, was proven effective for gradually introducing numerous defects and high non-metal heteroatoms into *A*-$Fe_2S_1N_5$/SNC. Specifically, a certain mass ratio of 2-benzimidazolethiol and melamine was first ground into a homogeneous mixture, which underwent confined pyrolysis in a flowing inert atmosphere (Fig. 1a). The thiol group on the 2-benzimidazolethiol was easily extracted by hydrogen to form free radicals due to its high activity. Through free radical reactions, the active C atom on melamine is likely covalently bonded with the thiol group to form C–S–C bonds. At high temperatures, melamine transforms into a carbon nitride structure (NC) and accompanied by the polymerization of NC frameworks, numerous defects spontaneously form[20]. During the thermal polymerization of 2-benzimidazolethiol, NC was encapsulated through a C–S–C bond linkage, and the constructed carbon framework was converted to S, N-codoped carbon nanosheets (SNC) after in situ restricted pyrolysis (Fig. 1b)[21]. In this matrix, sulfur was predominantly incorporated in the form of C–S–C. The presence of numerous sulfur-containing sites, coupled with the highly porous structure of the S–C, facilitated the preparation of diatomic iron catalysts with high loading through defect capture and sulfur tethering effects[22]. During the heating process, the edge S site formed by C–S bond breakage along with the adjacent N atom can effectively anchor individual Fe atoms through sulfur tethering and defect capture effects separately. Following initial anchoring, neighboring Fe atoms can migrate and interact with one another, resulting in the formation of a Fe–Fe bond on the surface of the graphene substrate. Finally, diatomic *A*-$Fe_2S_1N_5$/SNC catalysts were obtained at selected temperatures through carbonization reduction under an N_2 atmosphere (Fig. 1c). The mass percentage of Fe in the *A*-$Fe_2S_1N_5$/SNC catalysts was calculated to be 6.72 wt% through an inductively coupled plasma–optical emission (ICP–OES) test.

Scanning electron microscopy (SEM) revealed the curved and wrinkled nanosheet morphology of *A*-$Fe_2S_1N_5$/SNC (Fig. 2a and Supplementary Fig. 1), which was inherited from the SNC nanosheets (Supplementary Figs. 2, 3). The thickness of the nanosheets was calculated to be 4.5 nm (Supplementary Fig. 4). *A*-$Fe_2S_1N_5$/SNC consists of defect-rich thin nanosheets with many edge activity sites (Fig. 2b). The surface/edge defects can more easily anchor the metal, further changing the metal charge via atomic modulation strategies and affecting the electrocatalytic activity of the materials[23]. The energy-dispersive X-ray spectroscopy (EDS) images and electron energy loss spectroscopy (EELS) mapping of *A*-$Fe_2S_1N_5$/SNC at high magnification confirmed the uniform distribution of Fe, S, N, and C over the entire *A*-$Fe_2S_1N_5$/SNC (Fig. 2c and Supplementary Fig. 5). Furthermore, no obvious metal particles/clusters are observed in the high-angle annular dark-field scanning transmission electron microscopy (HAADF-STEM) image (Supplementary Fig. 6), indicating the atomically dispersed Fe in the SNC matrix[24]. Additionally, the morphologies of Fe_2N_6/NC, $Fe_1S_1N_3$/NC, and Fe_1N_4/NC are consistent with those of *A*-$Fe_2S_1N_5$/SNC (Supplementary Figs. 7–9). In Fig. 2d, aberration-corrected HAADF-STEM distinctly detects high-density and paired bright dots at the atomic level (circled by red dashed lines), corresponding to the atomically dispersed Fe–Fe atom pair. The ratio of Fe diatomic pairs is determined by counting the pair distance for more than 140 sites on the AC–STEM image of *A*-$Fe_2S_1N_5$/SNC (Supplementary Fig. 10), which reaches 80.7%. The intensity distribution along the X–Y direction in region A indicates that the spacing between the diatomic pair of Fe is ~0.25 nm (Fig. 2e), which closely matches the effective diameter of the Fe atoms

https://doi.org/10.1038/s41467-024-53871-5

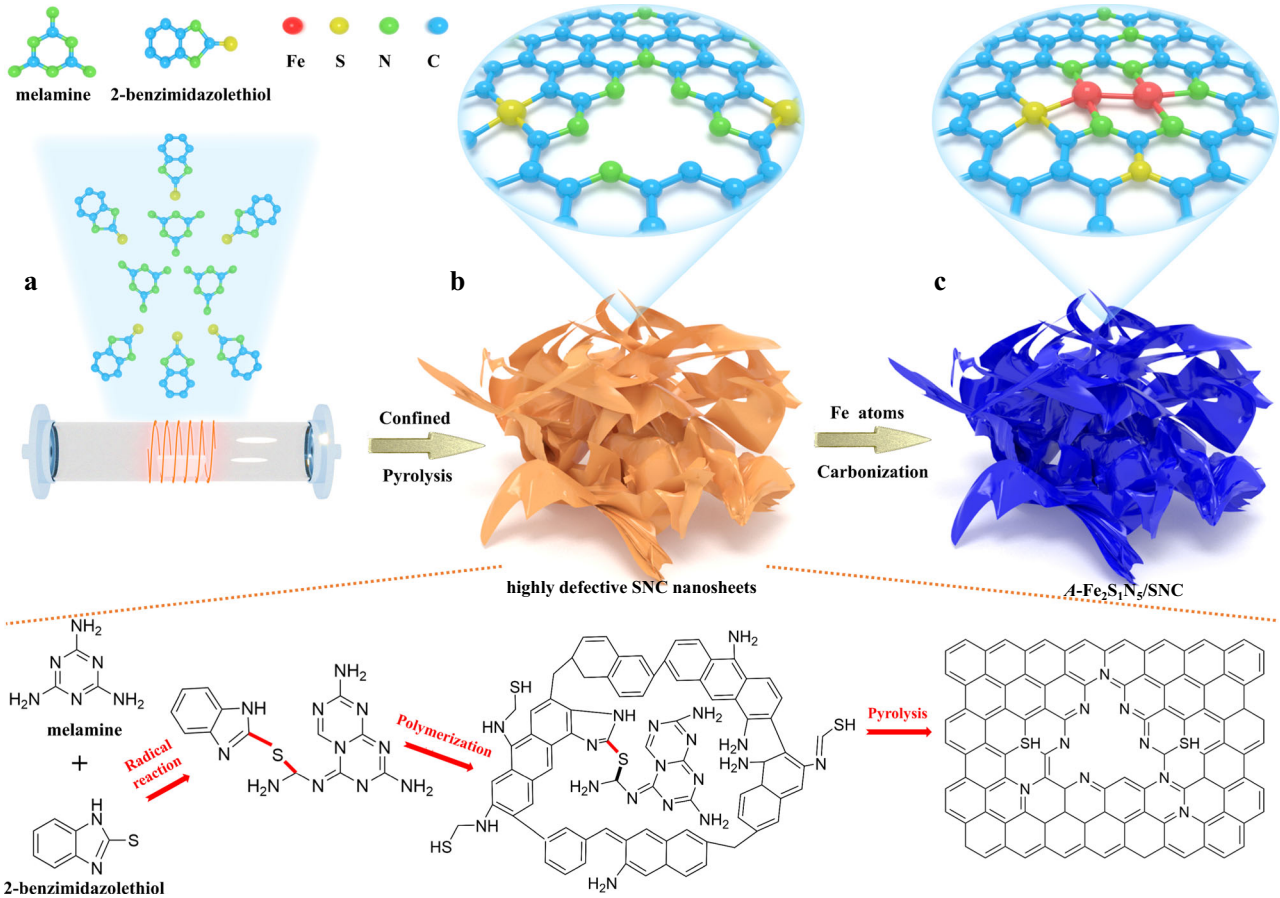

Fig. 1 | Two-step pyrolysis and carbonization synthesis process of *A*-$Fe_2S_1N_5$/SNC. a The certain mass ratio of 2-benzimidazolethiol and melamine underwent confined pyrolysis in a flowing inert atmosphere. **b** The free radical reactions, polymerization processes, and thermally induced decomposition of 2-benzimidazolethiol and melamine during pyrolysis were performed to synthesize highly defective SNC nanosheets. **c** The SNC anchored dual Fe atoms through sulfur tethering and defect capture effects.

in Fe_2N_6/NC (Supplementary Fig. 11). The EELS spectrum of small pixels of the annular dark field (red rectangle in Supplementary Fig. 5a) revealed visible signals of Fe, S, N, and C, confirming the densely populated FeS_1N_2–FeN_3 sites (Fig. 2f). Additionally, the relevant X-ray diffraction (XRD) and Raman characterization results are depicted in Supplementary Figs. 12, 13. N_2 adsorption and desorption isotherms (Supplementary Fig. 14 and Supplementary Table 1) revealed that the *A*-$Fe_2S_1N_5$/SNC, $Fe_1S_1N_3$/NC, Fe_2N_6/NC, Fe_1N_4/NC, and SNC catalysts had comparable Brunauer–Emmett–Teller (BET) specific surface areas. Pore size distribution analysis via the Barrett–Joyner–Halenda (BJH) model revealed a narrow peak at approximately 2.3 nm. The light element (i.e., C, N, S, H) contents of *A*-$Fe_2S_1N_5$/SNC were determined via CHNS analysis (Supplementary Table 2), which was consistent with the EDS analysis results. Furthermore, the ratio of Fe to S provides indirect evidence for the presence of Fe dual sites in *A*-$Fe_2S_1N_5$/SNC.

The electronic and atomic structural information for the Fe species in the samples was further examined via X-ray absorption spectroscopy (XAS). Figure 2g and Supplementary Fig. 15 show the Fe K-edge X-ray absorption near-edge structure (XANES) spectra of *A*-$Fe_2S_1N_5$/SNC, $Fe_1S_1N_3$/NC, Fe_2N_6/NC, and Fe_1N_4/NC. The adsorption threshold positions of *A*-$Fe_2S_1N_5$/SNC, $Fe_1S_1N_3$/NC, Fe_2N_6/NC, and Fe_1N_4/NC were both located between those of FeS_2 and Fe_2O_3, which indicates that the average metal valence states of the Fe species in *A*-$Fe_2S_1N_5$/SNC, $Fe_1S_1N_3$/NC, Fe_2N_6/NC, and Fe_1N_4/NC were situated between them[25]. From the XANES spectra shown in Supplementary Fig. 16, the average oxidation state of Fe in *A*-$Fe_2S_1N_5$/SNC obtained by fitting was 2.78. The Fourier transformed k^3-weighted extended X-ray absorption fine structure (EXAFS) data of *A*-$Fe_2S_1N_5$/SNC, $Fe_1S_1N_3$/NC, Fe_2N_6/NC, and Fe_1N_4/NC are displayed in Fig. 2h and Supplementary Fig. 17. The intense peak at 1.47 Å confirms the existence of a Fe–N scattering path in *A*-$Fe_2S_1N_5$/SNC, $Fe_1S_1N_3$/NC, Fe_2N_6/NC, and Fe_1N_4/NC. Concurrently, Fe–Fe interactions of ~2.27 Å are found in both *A*-$Fe_2S_1N_5$/SNC and Fe_2N_6/NC, suggesting that dual iron atoms exist in the form of direct bonding[26,27]. Notably, the peak appears at 1.84 Å in *A*-$Fe_2S_1N_5$/SNC, indicating the occurrence of Fe–S scattering. The atomic configurations of *A*-$Fe_2S_1N_5$/SNC, Fe_2N_6/NC, and Fe_1N_4/NC were subsequently studied via the Fe K-edge wavelet transform (WT)-EXAFS (Supplementary Fig. 18), which demonstrated the isolated characteristics of the Fe species[28]. The quantitative EXAFS fitting is studied to authenticate the local coordination configuration of Fe in *A*-$Fe_2S_1N_5$/SNC, $Fe_1S_1N_3$/NC, Fe_2N_6/NC, and Fe_1N_4/NC (Fig. 2i and Supplementary Figs. 19–22). The fitting results revealed that the coordination configurations of *A*-$Fe_2S_1N_5$/SNC, $Fe_1S_1N_3$/NC, Fe_2N_6/NC, and Fe_1N_4/NC are the FeS_1N_2-FeN_3, $Fe_1S_1N_3$, Fe_2N_6, and FeN_4 moieties, respectively. The first shell of *A*-$Fe_2S_1N_5$/SNC was fitted with Fe–N, Fe–S, and Fe–Fe backscattering paths. Coordination numbers of approximately 2.5, 0.5, and 1.0 were determined using Fe–N, Fe–S, and Fe–Fe in *A*-$Fe_2S_1N_5$/SNC, with average bond lengths of 1.90, 2.30, and 2.56 Å, respectively (inset of Fig. 2i and Supplementary Table 3). Furthermore, the atomic structure of *A*-$Fe_2S_1N_5$/SNC was evaluated by comparing the experimental spectra with the simulated XANES spectra. XANES calculations were conducted on FeS_1N_2–FeN_3 moieties with different Fe–S or C–S positions (Supplementary Fig. 23). It appears that the FeS_1N_2–FeN_3 structural motif with direct Fe–Fe bonding, one Fe bonded with one S

https://doi.org/10.1038/s41467-024-53871-5

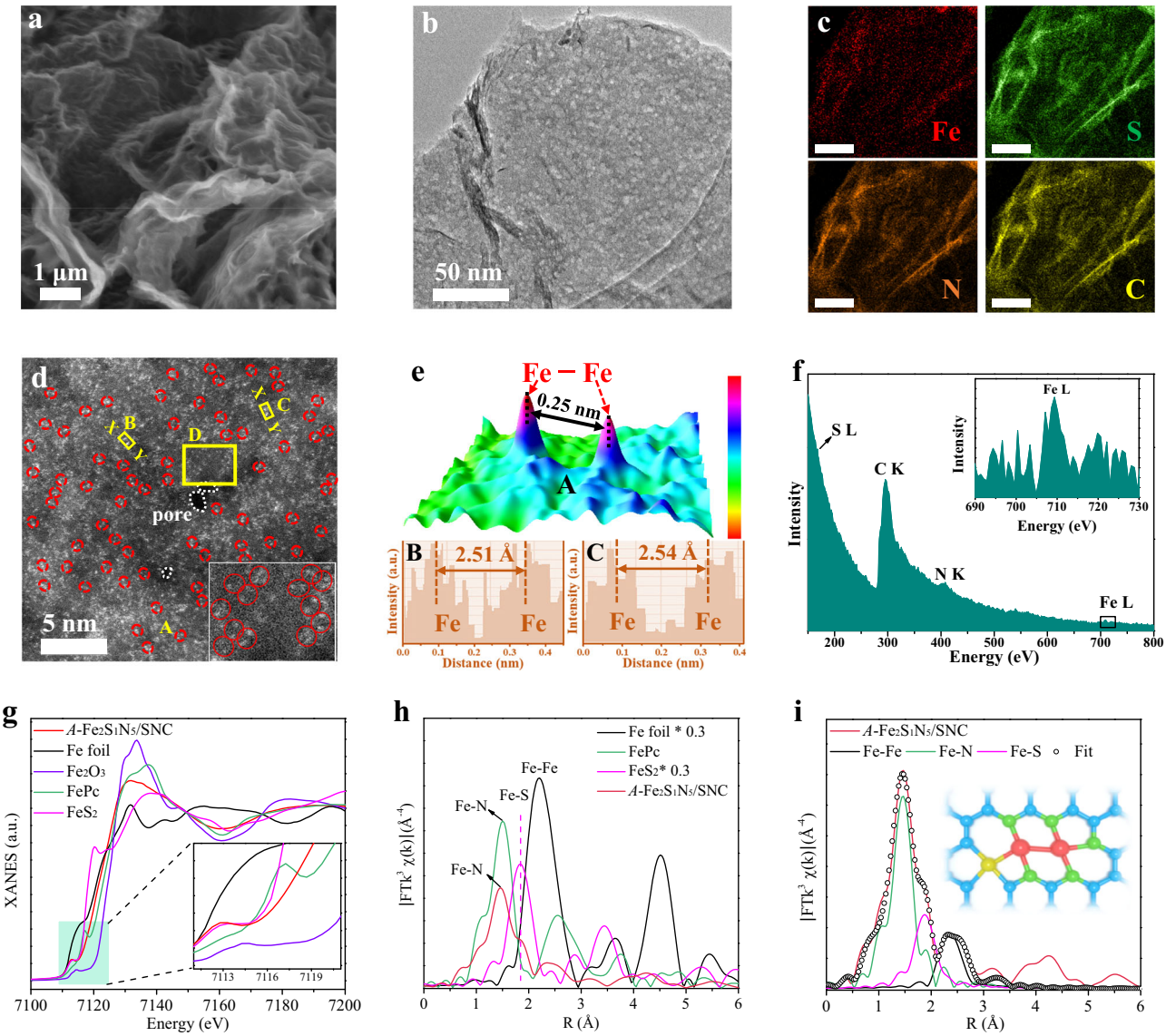

Fig. 2 | Morphology and atomic local structure characterization of *A*-$Fe_2S_1N_5$/SNC. a SEM; **b** HRTEM; and **c** EDS mapping images of Fe, S, N, and C for *A*-$Fe_2S_1N_5$/SNC (scale bar: 200 nm). **d** Aberration-corrected HAADF-STEM image of *A*-$Fe_2S_1N_5$/SNC. Inset: magnified region D, and the dual Fe sites are indicated by yellow ovals. **e** 3D model and the statistical Fe–Fe distance in the observed diatomic pairs A (top) and the intensity profile along the X–Y direction in regions B and C (bottom) of (**d**). **f** Electron energy loss spectroscopy (EELS) of *A*-$Fe_2S_1N_5$/SNC. **g** Fe K-edge XANES spectra (inset shows the magnified corresponding near-edge region), **h** FT K^3-weighted Fe K-edge EXAFS spectra, and **i** WT-EXAFS plots of *A*-$Fe_2S_1N_5$/SNC, Fe foil, FePc, and FeS_2. Inset **i**: atomic configuration model of *A*-$Fe_2S_1N_5$/SNC.

atom and two N atoms, and the other Fe connected by three N atoms in Supplementary Fig. 23a, is in good agreement with the experimental spectra. In addition, the C, N, and S types in the carbon matrix were confirmed by soft XAS and XPS spectra (Supplementary Figs. 24-29). It appears that π^* (C = C ring), π^* (C–N–Fe or C–S–Fe), and σ^* (C–C ring) exist in support of *A*-$Fe_2S_1N_5$/SNC, Fe_2N_6/NC, and Fe_1N_4/NC. Furthermore, three obvious peaks in the N K-edge soft XAS and N 1*s* XPS spectra for *A*-$Fe_2S_1N_5$/SNC, $Fe_1S_1N_3$/NC, Fe_2N_6/NC, Fe_1N_4/NC, and SNC represent the coexistence of pyridinic N, pyrrolic N, and graphitic N sites in the carbon matrix. Additionally, the C–S–N (C) species suggest the successful doping of the S atom into the NC fragment for *A*-$Fe_2S_1N_5$/SNC[29]. The Fourier transform infrared (FTIR) spectrum of the *A*-$Fe_2S_1N_5$/SNC catalyst (Supplementary Fig. 30) revealed all the non-metallic bonds that constitute the basic framework of the catalyst[30]. The NH_3-TPD technique was used to titrate the acidic sites. As shown in Supplementary Fig. 31, negligible acidic sites were found across the *A*-$Fe_2S_1N_5$/SNC catalyst. These results indicate that N and S are doped into the structure of graphene[31].

Electrocatalytic OER performance of *A*-$Fe_2S_1N_5$/SNC

To evaluate the alkaline OER electrocatalytic performance of *A*-$Fe_2S_1N_5$/SNC, we conducted electrochemical measurements in a 1.0 M KOH solution via a standard three-electrode configuration. The obtained *A*-$Fe_2S_1N_5$/SNC displayed more obvious advantages (Fig. 3a) in terms of overpotential (193 mV at 10 mA cm^{-2}) than the $Fe_1S_1N_3$/NC (263 mV), Fe_2N_6/NC (280 mV), Fe_1N_4/NC (369 mV), SNC (409 mV), NC (437 mV), and even RuO_2 (255 mV). The optimal amount of Fe source was identified by the OER activities, and the results showed that the catalyst exhibited the optimized performance when the amount of iron (III) chloride was 40 mg (Supplementary Fig. 32). The corresponding LSV curves without *iR* compensation for the catalysts are shown in Supplementary Fig. 33. The *A*-$Fe_2S_1N_5$/SNC catalyst delivered a superior Tafel slope compared to $Fe_1S_1N_3$/NC, Fe_2N_6/NC, Fe_1N_4/NC, SNC, and RuO_2, suggesting faster OER kinetics (Supplementary Fig. 34a)[32]. Notably, *A*-$Fe_2S_1N_5$/SNC was the most active OER electrocatalyst among the reported SAC/DAC catalysts (Supplementary Fig. 34 and Supplementary Table 5), which might be attributed to the

https://doi.org/10.1038/s41467-024-53871-5

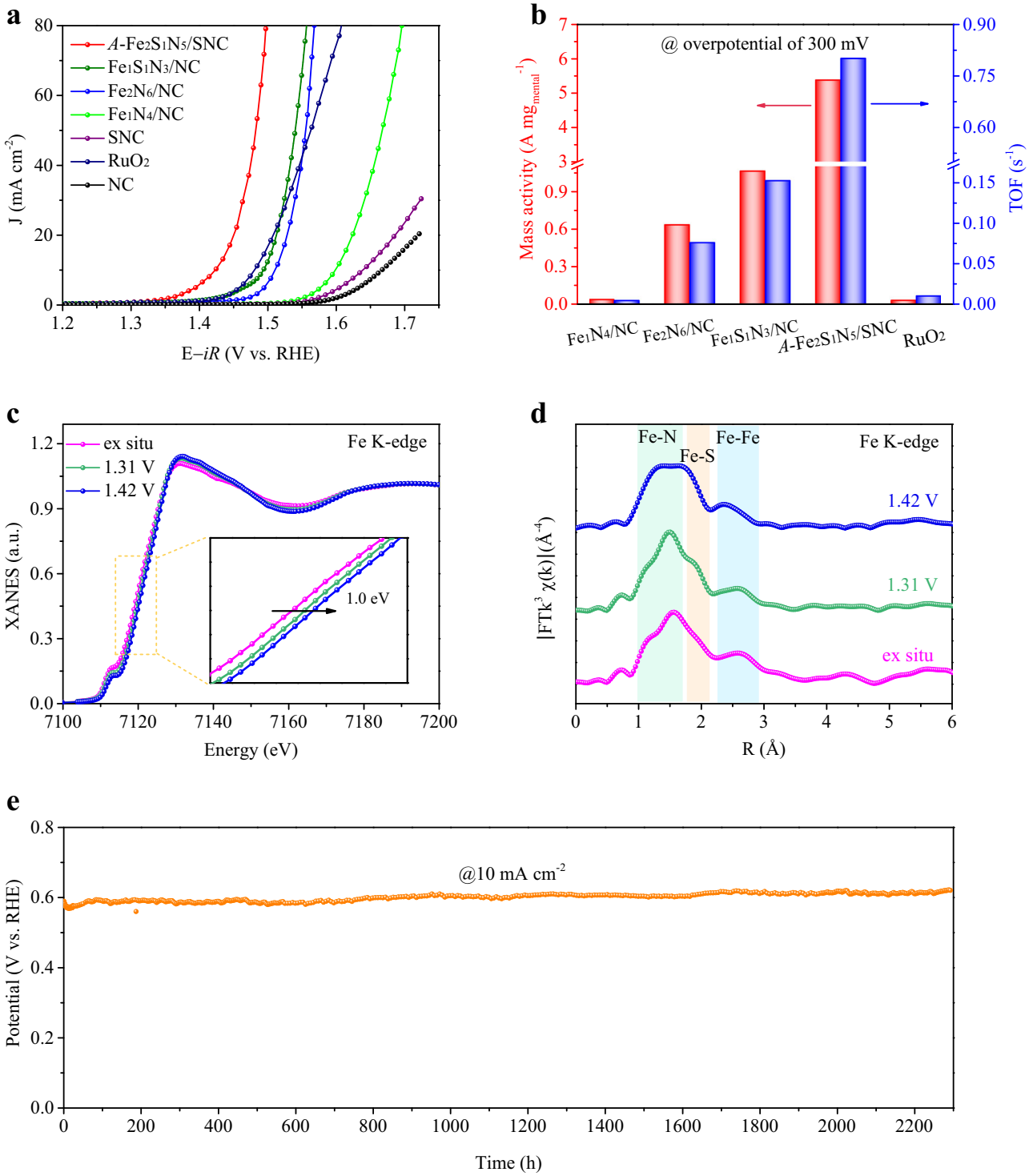

Fig. 3 | OER electrochemical activity and in situ XAFS characterization of *A*-$Fe_2S_1N_5$/SNC in 1.0 M KOH. a LSV curves of the prepared catalysts. Note: the geometric surface area is 1.0 cm^2; series resistance (*Rs*) are 2.7, 3.6, 4.5, 5.6, and 8.1 Ω for *A*-$Fe_2S_1N_5$/SNC, $Fe_1S_1N_3$/NC, Fe_2N_6/NC, Fe_1N_4/NC, and SNC, respectively. **b** TOF and mass activity at 300 mV, **c** normalized XANES spectra at the Fe K-edge for the OER (the insets are magnified images of the near-edge region for the OER), **d** k^3-weighted FT-EXAFS at ex situ, 1.31, and 1.42 V vs. RHE (the shaded area highlights the shifts in the peak positions of Fe–N, Fe–S, and Fe–Fe in the first coordination shell), **e** chronopotentiometric measurement of *A*-$Fe_2S_1N_5$/SNC at 10 mA cm^{-2} (no *iR*-correction).

asymmetric iron dual-atom sites. The electrochemically active surface area (ECSA) represents the actual number of active sites of the electrocatalytic catalysts, which was evaluated through the double-layer capacitance (C_{dl}) of the catalysts[33]. As derived from cyclic voltammograms at various sweep rates (Supplementary Fig. 35), the ECSA and C_{dl} of *A*-$Fe_2S_1N_5$/SNC were significantly greater than those of $Fe_1S_1N_3$/NC, Fe_2N_6/NC, Fe_1N_4/NC, and SNC (Supplementary Fig. 36 and Supplementary Table 4), confirming that the asymmetric configuration in *A*-$Fe_2S_1N_5$/SNC possessed more exposed reactive sites and hence enhanced the OER activity[34,35]. To further determine whether the enhanced OER activity is solely contingent on the increased number of active sites, the ECSA-normalized OER polarization curves were

calculated. From the ECSA-normalized LSV curves (Supplementary Fig. 37a), the *A*-$Fe_2S_1N_5$/SNC catalyst still exhibited the highest activity, suggesting intrinsically improved OER activity on the *A*-$Fe_2S_1N_5$/SNC catalyst due to the presence of asymmetric iron dual-atom sites[36]. Electrochemical impedance spectroscopy (EIS) is a common indicator used to probe the interface resistance change between a catalyst electrode and an electrolyte[37]. As illustrated in Supplementary Fig. 37b, the *A*-$Fe_2S_1N_5$/SNC catalyst exhibited a lower charge transfer resistance than the Fe_2N_6/NC catalyst. This suggests an accelerated charge-transfer mechanism following the addition of sulfur after S doping during the OER. Furthermore, the SNC support demonstrated a diminished charge transfer resistance relative to that of the NC support, indicating an increased electron-transfer rate within the SNC framework. As a result, the incorporation of the S dopant has been shown to increase the efficiency of charge transfer during the alkaline OER[38]. The intrinsic catalytic activity of the catalysts was subsequently assessed by the calculated turnover frequency (TOF) shown in Fig. 3b, Supplementary Fig. 38a, and Supplementary Note 1. Notably, the *A*-$Fe_2S_1N_5$/SNC catalyst displayed an extremely high TOF throughout the entire overpotential window. In general, the TOF values for *A*-$Fe_2S_1N_5$/SNC were as high as 2875.0 O_2 h^{-1} at an overpotential of 300 mV, 11 times and 183 times greater than those of Fe_2N_6/NC (273.0 O_2 h^{-1}) and Fe_1N_4/NC (15.7 O_2 h^{-1}), respectively. In addition, the mass activities (MA) of *A*-$Fe_2S_1N_5$/SNC were also greater than those of $Fe_1S_1N_3$/NC, Fe_2N_6/NC, and Fe_1N_4/NC (Supplementary Fig. 38b and Supplementary Note 2), demonstrating the high-intrinsic catalytic activity of *A*-$Fe_2S_1N_5$/SNC[39]. The Faradaic efficiency (FE) was calculated in comparison to the amount of oxygen produced experimentally against the theoretical quantity. The FE of *A*-$Fe_2S_1N_5$/SNC was approximately 99.1% (Supplementary Fig. 39 and Supplementary Note 3), indicating that no side reactions occurred during the OER process. In addition, we evaluated the OER catalytic performance of the *A*-$Fe_2S_1N_5$/SNC under the industrial electrolytic water system (such as 80 °C, 30% KOH), and the results revealed that *A*-$Fe_2S_1N_5$/SNC has potential for industrial application (Supplementary Fig. 40).

An in situ XAFS analysis was performed to elucidate the structural evolution and real-time change in the Fe chemical state during the OER[40,41]. A homemade cell was used to perform the in situ XAS tests (Supplementary Fig. 41) through the commonly used Lytle detector (in fluorescence mode) to collect all the spectra. As shown in Fig. 3c, the Fe K-edge absorption edge gradually shifted to higher energy, accompanied by an increase in the applied potential from ex situ conditions to 1.42 V vs. RHE, indicating that the average valence state of the Fe sites increased as the OER proceeded[42,43]. The formation of higher valence Fe could be further supported by the first derivative XANES curves in Supplementary Fig. 42. To further probe the evolution of the coordination configuration for the Fe atoms in *A*-$Fe_2S_1N_5$/SNC, FT–EXAFS spectra were recorded at the Fe K-edges (Fig. 3d), the Fe–N, Fe–S, and Fe–Fe shells displayed obvious dynamic changes during the OER. The coordination peaks shift to the low-R region, which might be derived from bridging adsorption of the oxygen-containing intermediates (i.e., O*, OH*, OOH*) on dual Fe sites[44]. By considering the Fe–N, Fe–S, Fe–Fe, and Fe–O scattering paths, the first coordinated shell of the EXAFS curve-fitting analysis for *A*-$Fe_2S_1N_5$/SNC is displayed in Supplementary Figs. 43, 44 and Supplementary Table 7. Accordingly, slight shrinkage of the Fe–N bond length could fix the dual Fe sites during the OER, thus avoiding possible dissolution and improving stability[45].

The *A*-$Fe_2S_1N_5$/SNC electrode exhibited electrochemical durability after 2000 h of continuous operation under constant current test conditions (10 mA cm^{-2}) with >97% retention (Fig. 3e), which demonstrated its feasibility in industrial applications[46]. The stability of *A*-$Fe_2S_1N_5$/SNC was also validated via LSV curves before and after 50000 CV cycles (with no loss) (Supplementary Fig. 45). A comparison of the long-term OER durability of *A*-$Fe_2S_1N_5$/SNC and other reported electrocatalysts is summarized in Supplementary Fig. 46 and Supplementary Table 5. Undoubtedly, *A*-$Fe_2S_1N_5$/SNC was one of the most stable reported OER catalysts. The morphology and structure of *A*-$Fe_2S_1N_5$/SNC after the durability tests were examined via TEM, XRD, Raman, and XPS analyses (Supplementary Figs. 47, 48), which revealed negligible changes. After cyclic testing, the ICP results revealed that the Fe content in *A*-$Fe_2S_1N_5$/SNC remained at 97.9%, confirming the stability of the catalyst (Supplementary Table 6 and Supplementary Note 5).

To determine the universality of the synthesis method, several other 3D transition-metal (for example, M = Co [6.43 wt%], Cu [7.15 wt%], Ni [6.98 wt%], and Mn [7.01 wt%]) diatomic *A*-$M_2S_1N_5$/SNC catalysts were produced (Supplementary Fig. 49). As demonstrated in Supplementary Figs. 50–53, *A*-$M_2S_1N_5$/SNC possesses a thin and curly nanosheet morphology with no obvious metal particles. In the AC HAADF–STEM image, many dense dimers are observed, indicating the presence of metal dual-atom pairs in *A*-$M_2S_1N_5$/SNC. The unsymmetrically arranged MS_1N_2–MN_3 coordination configuration was further confirmed by XAS spectra and quantitative EXAFS fittings (Supplementary Figs. 54–60 and Supplementary Table 8). The corresponding OER performance of *A*-$M_2S_1N_5$/SNC is also shown in Supplementary Fig. 61. The successful preparation of *A*-$M_2S_1N_5$/SNC demonstrates the feasibility and scalability of the strategy proposed in this paper for preparing asymmetric homonuclear diatomic catalysts, providing potential for the industrialization of diatomic catalysts.

Theoretical study of *A*-$Fe_2S_1N_5$/SNC for the OER

To elucidate the mechanism of the oxygen electrochemical reaction on the asymmetrical *A*-$Fe_2S_1N_5$/SNC catalyst in comparison with those on the Fe_2N_6/NC and $Fe_1S_1N_3$/NC catalysts, the first-principles method was adopted to study their proton-coupling electron-transfer (PCET) processes[47]. Supplementary Figs. 62–65 show the possible configurations of the Fe_2N_6/NC and *A*-$Fe_2S_1N_5$/SNC catalysts. Given the spin-polarized Fe, the relative energies between the ferromagnetic (FM) and anti-ferromagnetic (AFM) states for each model and the formation energies were systematically evaluated to confirm the ground states of the stable models. The Fe_2N_6/NC and *A*-$Fe_2S_1N_5$/SNC models were all AFM ground states, and the two Fe atoms were named the Fe-1 and Fe-2 sites for ease of distinction. The Fe-2 site connects with one S atom and two N atoms, and the Fe-1 site coordinates with only N atoms in the asymmetrical *A*-$Fe_2S_1N_5$/SNC model. The $Fe_1S_1N_3$/NC model is depicted in Supplementary Fig. 66. Initially, the adsorption of intermediates in the OER/ORR was evaluated with these models, and the corresponding adsorbed configurations and adsorption-free energies are shown in Supplementary Figs. 67–69, Supplementary·Data 1, and Supplementary Tables 9–11, respectively. The O and OH species have strong binding energies of −0.64 and −1.49 eV on the bare *A*-$Fe_2S_1N_5$/SNC surface, −0.44 and −1.25 eV on the bare Fe_2N_6/NC surface, and 1.62 and 0.49 eV on the bare $Fe_1S_1N_3$/NC catalyst, respectively, all deviating from the ideal adsorption energies of the optimal OER/ORR catalyst, with values of 2.46 and 1.23 eV; this indicated that the O or OH intermediates were prone to occupy the Fe sites in the electrochemical surroundings[48]. The Pourbaix diagram clearly shows the stable states of the catalyst surface under electrochemical conditions, which are related to the pH and electrode potential[49]. Figure 4a and Supplementary Fig. 70 depict the free energies of a series of coverage surfaces following electrode potential U vs. RHE sampling for the *A*-$Fe_2S_1N_5$/SNC, Fe_2N_6/NC, and $Fe_1S_1N_3$/NC models. Under real electrochemical OER conditions, such as 1.50 V vs. RHE, their surfaces were covered by 3O with two Fe sites for diatomic catalysts and 2OH for the $Fe_1S_1N_3$/NC catalyst, termed 3O-$Fe_2S_1N_5$/SNC, 3O-Fe_2N_6/NC, and 2OH-$Fe_1S_1N_3$/NC in the OER surroundings, respectively. According to the OER mechanism of single-atom catalysts reported by Pacchioni et al.[50], at least one unconventional chemical intermediate, such as 2*OH, *O + *OH, 2*O, or *O_2 ("*" marks the surface site), was found to be more

https://doi.org/10.1038/s41467-024-53871-5

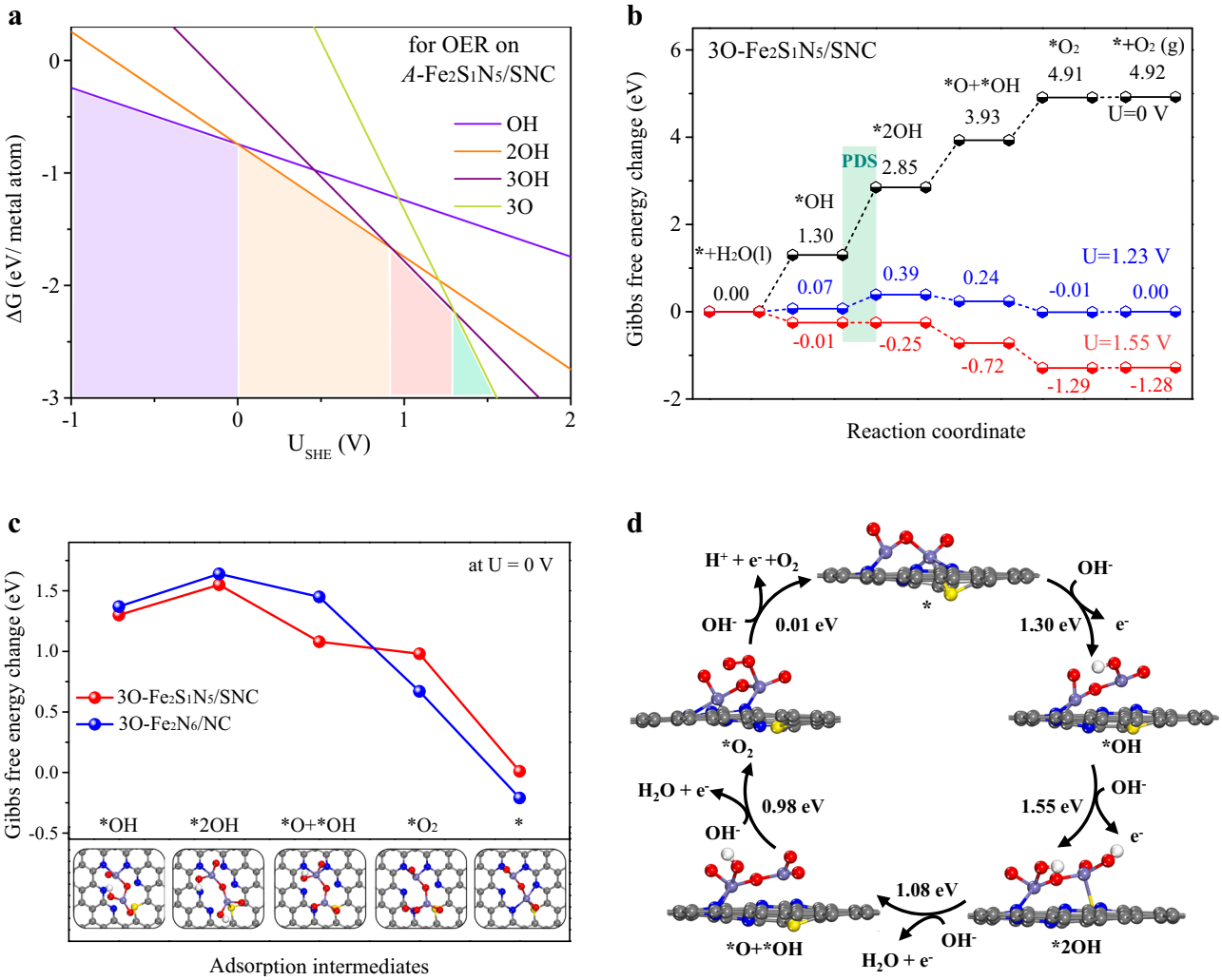

Fig. 4 | Mechanistic exploration of *A*-$Fe_2S_1N_5$/SNC for the OER. a Free energy of a series of coverage fraction surfaces sampled for the *A*-$Fe_2S_1N_5$/SNC catalysts; **b** The corresponding free energy change of the OER at the Fe−2 site; **c** comparison of Gibbs free energy changes of the OER intermediates in *A*-$Fe_2S_1N_5$/SNC and Fe_2N_6/NC at U = 0 V; **d** the proposed 4e⁻ mechanism of the OER on *A*-$Fe_2S_1N_5$/SNC.

stable than the classical intermediate, including *O and *OOH species, in all cases. Therefore, we systematically evaluated the adsorption of these OER intermediates, which are composed of classical and unconventional intermediates, on the abovementioned surfaces, and the corresponding optimized adsorption configurations and adsorption energies are displayed in Supplementary Figs. 71–73, Tables 12–14, and Supplementary·Data 2. The Gibbs free energy changes of the elementary steps of the OER are depicted in Fig. 4b, c and Supplementary Figs. 74–77. The unconventional complex (*O + *OH) was more stable than the classical *OOH intermediate at the Fe−2 site of the 3O-$Fe_2S_1N_5$/SNC and 3O-Fe_2N_6/NC surfaces and had similar adsorption energies of *2OH and *O. Hence, their cascade OER processes on the diatomic catalyst could proceed through unconventional intermediates: H_2O (l)→*OH → *2OH → *O + *OH → $*O_2$ → O_2 (g). Considering the instability of the 2OH-$Fe_1S_1N_3$/NC catalyst induced by the unusual intermediates *2OH and *O + *OH, the classical steps were considered only for the OER process. Compared with the symmetric 3O-Fe_2N_6/NC catalyst with an overpotential of 0.41 V, the asymmetric diatomic catalyst 3O-$Fe_2S_1N_5$/SNC had the lowest overpotential (0.32 V) when an S source was used, and it also excelled with the single-atom catalyst 2OH-$Fe_1S_1N_3$/NC (0.35 V), which was consistent with the experimental measurements. Their potential-determined steps (PDSs) were the second dehydrogenation process [*OH → *2OH (O)]. Figure 4d depicts the OER mechanism on the 3O-$Fe_2S_1N_5$/SNC catalyst in light of unusual intermediates. The overpotentials of the classical intermediates for the OER [H_2O (l)→*OH → *O → *OOH → O_2 (g)] were 0.32, 0.44, and 0.35 V with the same PDSs of *OH → *O for 3O-$Fe_2S_1N_5$/SNC, 3O-Fe_2N_6/NC, and 2OH-Fe_1SN_3/NC, respectively. For both classical and unconventional intermediates, *A*-$Fe_2S_1N_5$/SNC exhibited optimal electrochemical OER performance. The above OER results were based on an implicit solvent model (VASPsol), which can generally capture electrostatic interactions with diverse intermediates and neglect the influence of hydrogen bonds on their stabilization and consequent OER mechanism via an explicit solvent model[51].

The improved OER performance of 3O-$Fe_2S_1N_5$/SNC was attributed mainly to the enhanced oxygen capture ability induced by the involvement of an unsymmetric S source and dual-atom Fe sites. The Crystal Orbital Hamilton Population (COHP) results of the adsorbed O species between O and the active Fe site on the diatomic catalyst are shown in Supplementary Fig. 78. The 3O-$Fe_2S_1N_5$/SNC surface possessed stronger bond strength, with a more negative integrated COHP (ICOHP) value of −2.17 for the spin-up state and −3.44 for the spin-down state, which was principally due to Fe $3d_{yz}$ and O $2p_z$, Fe $3d_{xy}$, and O $2p_x$, than that of 3O-Fe_2N_6/NC, with ICOHP values of −2.13 and −3.35, respectively. The charge and spin magnetic moment distributions of the active sites also play critical roles in the OER[52,53], as simulated by the

https://doi.org/10.1038/s41467-024-53871-5

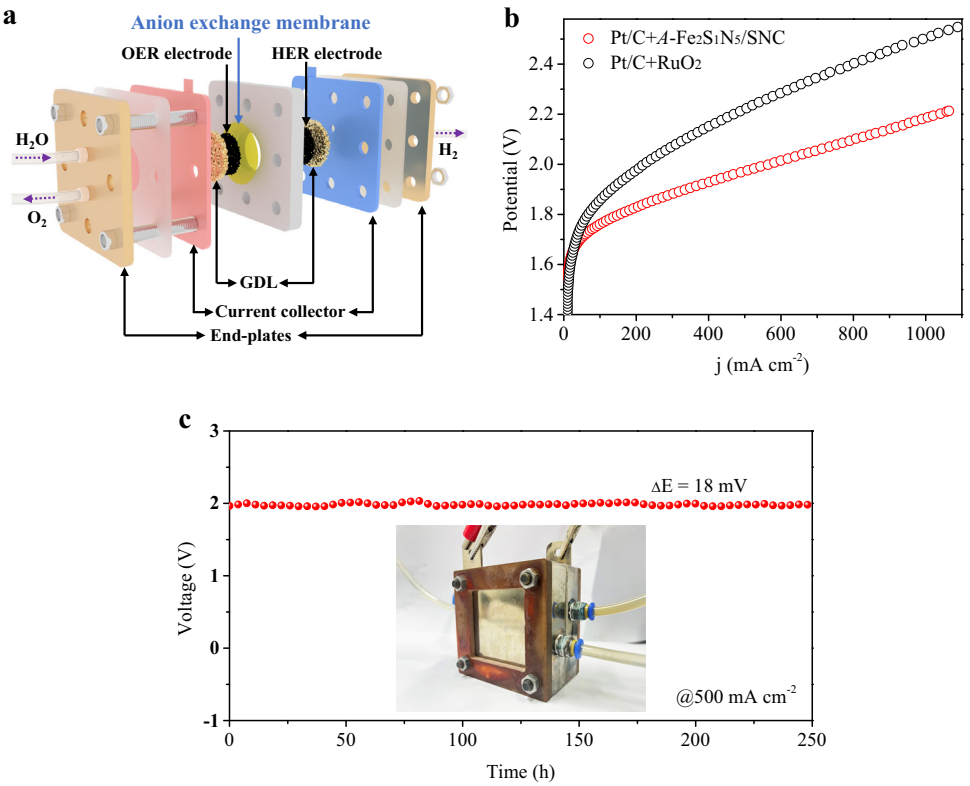

Fig. 5 | Performance of AEMWE devices. a Schematic illustration of the assembled AEM electrolyzer (GDL, gas diffusion layer); **b** polarization curves of the AEMWE electrolyzer using *A*-$Fe_2S_1N_5$/SNC and commercial Pt/C; **c** chronopotentiometry test of the AEMWE utilizing *A*-$Fe_2S_1N_5$/SNC held at 500 mA cm^{-2}. Inset **c**: Digital image of the AEMWE electrolyzer.

Bader charge, differential charge, and spin-charge densities in Supplementary Figs. 79–80. For 3O-$Fe_2S_1N_5$/SNC, the Fe-1 site reduced much more electrons (+1.52 e^-) to surrounding coordinate atoms than that of the Fe-2 site (+1.48 e^-) to generate localized spontaneous electric polarization, yet the Fe-2 site possessed a larger magnetic moment (MM: 3.82 μ_B) than the Fe-1 site (3.60 μ_B), in contrast with the symmetrical 3O-Fe_2N_6/NC model for the Fe-1 and Fe-2 sites featuring the same charge (+1.53 e^-) and magnetic moment (3.72 μ_B) distributions. Even though the obtained charge (+1.40 e^-) and MM (2.85 μ_B) of the Fe site on the 2OH-$Fe_1S_1N_3$/NC catalyst were less than those of the symmetrical 3O-Fe_2N_6/NC, the derived electric polarization induced by the introduction of the S source into the FeN_4 moiety significantly increased the OER performance. Above all, the spontaneous electric polarization intensity endowed by heteroatom S doping and dual-atom sites can synergistically optimize the adsorption capability of OER intermediates, thus promoting the electrochemical oxygen evolution property.

Similarly, for the electrochemical ORR, such as 0.90 V vs. RHE, their surfaces were covered by 2OH species, named 2OH-$Fe_1S_1N_3$/NC, 2OH-Fe_2N_6/NC, and 2OH-$Fe_2S_1N_5$/SNC. Supplementary Figs. 73, 81, 82 display the optimized ORR intermediates, and the corresponding adsorption energies are shown in Supplementary Tables 14–16. Supplementary Fig. 83 shows the free energy changes of the ORR mechanism on these surfaces. The asymmetric diatomic 2OH-$Fe_2S_1N_5$/SNC catalyst had the largest onset potential (0.79 V) among those of 2OH-Fe_2N_6/NC (0.54 V) and 2OH-$Fe_1S_1N_3$/NC (0.65 V)[54], which matches well with the experimental results; their PDSs constitute the first hydrogenation step for the generation of *OOH species. The enhanced capture of OOH species was attributed to the large charge and spin magnetic moment population of the active Fe site, specifically for the asymmetric 2OH-$Fe_2S_1N_5$/SNC catalyst, as shown in Supplementary Fig. 84. Above all, the unsymmetrical geometric construction of the *A*-$Fe_2S_1N_5$/SNC catalyst realized spontaneous electric polarization via the coupling of dual-site and heteroatom S doping to achieve disparate OER/ORR performance.

AEMWE device performance of *A*-$Fe_2S_1N_5$/SNC

We further assembled an alkaline AEMWE (anion exchange membrane water electrolyzer) catalyzed by *A*-$Fe_2S_1N_5$/SNC, as shown in Fig. 5a. The *A*-$Fe_2S_1N_5$/SNC-based cell displayed better performance: a current density of 500 mA cm^{-2} was reached at 1.94 V, whereas an even higher current density of 1.0 A cm^{-2} was reached at 2.18 V. In contrast, the current density of the RuO_2||Pt/C cell at 2.22 V was 500 mA cm^{-2} (Fig. 5b). Consequently, compared with those catalyzed by precious metal electrocatalysts, the performance of the AEM electrolyzer catalyzed by *A*-$Fe_2S_1N_5$/SNC was improved. To provide a comprehensive assessment of the alkaline electrolyzer enabled by *A*-$Fe_2S_1N_5$/SNC, as shown in Supplementary Table 17, the performance of the AEM electrolyzer using the *A*-$Fe_2S_1N_5$/SNC electrocatalyst exceeded that of most of the reported state-of-the-art catalysts. To characterize the stability of the electrolyzer, when assembled with *A*-$Fe_2S_1N_5$/SNC, the AEM electrolyzer could operate at 500 mA cm^{-2} for at least 250 h with a negligible increase in voltage (Fig. 5c). Furthermore, the catalytic performances of the ORR (Supplementary Figs. 85–89) and the zinc-air battery (ZAB) were tested to validate the potential application of the bifunctional *A*-$Fe_2S_1N_5$/SNC catalyst. As depicted in Supplementary Fig. 90, the performance of the *A*-$Fe_2S_1N_5$/SNC-based battery is superior to that of the Pt/C + RuO_2 battery, which indicates its potential in commercial applications for *A*-$Fe_2S_1N_5$/SNC-based devices.

Discussion

In summary, a general and scalable approach for the synthesis of a series of *A*-DACs (*A*-$M_2S_1N_5$/SNC) with high metal loading is achieved. *A*-$Fe_2S_1N_5$/SNC exhibits outstanding OER catalytic performance due to

the presence of asymmetric FeS_1N_2–FeN_3 moieties, indicating high AEMWE and ZAB potential. For the OER, *A*-$Fe_2S_1N_5$/SNC delivers a low overpotential of 193 mV at 10 mA/cm^2 under alkaline conditions, which is higher than those reported for diatomic catalysts and commercial RuO_2. Furthermore, *A*-$Fe_2S_1N_5$/SNC is stable for more than 2000 h at 10 mA cm^{-2}, which suggests that the durability and catalytic activity can be balanced for the *A*-$Fe_2S_1N_5$/SNC electrocatalyst. The AEMWE device with *A*-$Fe_2S_1N_5$/SNC catalysts also afforded durability for up to 250 h at 500 mA cm^{-2} and exhibited an industrially required current density of 1.0 A cm^{-2} at 2.18 V. For *A*-$Fe_2S_1N_5$/SNC, high activity comes from the cocatalysis of a high-density active Fe–Fe site and high stability derives from the regulation of the metal atom microenvironment by S coordination. As corroborated by our operando characterizations and DFT calculations, unique configurations yield the optimal adsorption/desorption energy on Fe–Fe sites for a radical intermediate with a reduced reaction barrier. We expect that this strategy will contribute to the promotion of the application of diatomic catalysts in the production of clean energy through water electrolysis.

Methods

Chemicals

Melamine (>99%, Aladdin), iron (III) chloride (>99%, Sigma-Aldrich), ruthenium (IV) oxide (99.9%, Aladdin), 2-benzimidazolethiol (>99%, Aladdin), trimesic acid (>98%, Aladdin), dicyandiamide (>99%, Sigma-Aldrich), ethanol (>99.5%, Aladdin), potassium hydroxide (95%, Aladdin), nafion117 solution (~5% in a mixture of lower aliphatic alcohols and water, Aladdin), commercial Pt/C (20 wt% metal, Aladdin), and carbon cloth (CC, type: WOS1009, thickness: 0.33 mm). All chemical reagents were utilized as received. The purity of oxygen and nitrogen gas is 99.999%.

Synthesis of SNC and NC

In a standard synthesis of sulfur and nitrogen co-doped carbon nanosheets, a mixture of 2-benzimidazolethiol and melamine in precise mass ratios (1:7) was initially milled to obtain a homogeneous precursor. The precursor was subsequently subjected to thermal polymerization and carbonization in a flowing nitrogen atmosphere within a horizontally aligned quartz tube, with a heating rate of 2 °C min^{-1} until reaching 1000 °C, which was maintained for a duration of 2 h. The final synthesized product is designated as SNC, whereas the NC support was prepared using the same methodology as SNC, with the significant exception that the sulfur source (2-benzimidazolethiol) was excluded.

Synthesis of *A*-$Fe_2S_1N_5$/SNC

To prepare the *A*-$Fe_2S_1N_5$/SNC, the obtained SNC nanosheet support was ultrasonicated in 10 mL of ethanol, and then 40 mg of iron (III) chloride, 1.0 g of dicyandiamide, and 0.1 g of trimesic acid were added to the above suspension and stirred vigorously for 30 min. The suspension was then evaporated to dry the solvent in a rotary evaporator to obtain a gray powder. The gray powder was annealed at 900 °C (heating rate of 2 °C min^{-1}) and held for 3 h under high-purity nitrogen. After naturally cooling to room temperature, black *A*-$Fe_2S_1N_5$/SNC nanosheets were obtained.

Synthesis of Fe_2N_6/NC, $Fe_1S_1N_3$/NC, and Fe_1N_4/NC

To prepare the Fe_2N_6/NC, the obtained NC nanosheet support was ultrasound dispersion in 10 mL of ethanol, then 40 mg iron (III) chloride, 1.0 g dicyandiamide, and 0.1 g trimesic acid were added into the above suspension and stirred vigorously for 30 min. The suspension was then evaporated to dry the solvent in a rotary evaporator to obtain a gray powder. The gray powder was annealed at 900 °C with a heating rate of 2 °C min^{-1} and maintained for 2 h under the N_2 atmosphere. After naturally cooling to room temperature, the black Fe_2N_6/NC nanosheets were obtained.

To obtain Fe_1N_4/NC, directly add 40 mg of iron (III) chloride, 1.0 g dicyandiamide, and 0.1 g trimesic acid to 15 mL of ethanol and vigorously stir for 30 min. The suspension was then evaporated to dry the solvent in a rotary evaporator to obtain a gray powder. The gray powder was annealed at 900 °C with a heating rate of 2 °C min^{-1} and maintained for 2 h under the N_2 atmosphere. After naturally cooling to room temperature, the black Fe_1N_4/NC was obtained.

The synthesized NC nanosheet support was subjected to ultrasonic dispersion in 10 mL of ethanol. Subsequently, 40 mg of iron (III) chloride, 0.5 mL of thiophene, 1.0 g of dicyandiamide, and 0.1 g of trimesic acid were incorporated into the suspension, which was then stirred vigorously for 30 min. The solvent was subsequently removed through evaporation using a rotary evaporator, yielding a gray powder. This gray powder was then subjected to annealing at 900 °C, with a heating rate of 2 °C min^{-1}, and maintained at this temperature for 3 h in an atmosphere of high-purity nitrogen. Following natural cooling to ambient temperature, the resultant black $Fe_1S_1N_3$/NC was obtained.

General synthesis of *A*-$M_2S_1N_5$/SNC. (M = Co, Cu, Ni, and Mn). For the *A*-$M_2S_1N_5$/SNC (M = Co, Cu, Ni, and Mn), the preparation process is the same as *A*-$Fe_2S_1N_5$/SNC catalyst, except that the use of metal salts is 0.25 mmol cobalt (II) chloride, copper (II) chloride, nickel (II) chloride, and manganese (II) chloride, respectively.

Characterizations

X-ray diffraction (XRD, D8 Bruker AXS, scan range of 10–80°) test was performed to identify the crystallinity and phase of samples. Raman (Lab RAM HR Evolution spectrometer, excitation line of 532 nm) was analyzed to record the stretching and bond vibration modes. The XPS data were acquired using an Escalab 250Xi instrument, employing magnesium and aluminium as the excitation sources from Kratos Analytical. The data were converted to VAMAS file format and subsequently imported into Avantage software for peak fitting analysis. Binding energies reported herein are referenced to the C (1*s*) signal at 284.5 eV. The methodology for preparing XPS samples involves the following steps: First, a small quantity of the powder sample is positioned on a piece of aluminum foil. Subsequently, a section of double-sided Scotch tape, ~5 × 5 mm^2 in area, is cut and held with tweezers to adhere the sample. The tape, along with the sample, is then subjected to gentle pressure using a tablet press until the sample surface is rendered flat and free of contaminants. Finally, the prepared sample is placed on the sample stage for analysis. Scanning electron microscopy (SEM) data were obtained using an Ultra 55 Zeiss instrument to examine the morphology of the samples. Transmission electron microscopy (TEM) and high-resolution transmission electron microscopy (HRTEM) analyses were performed on an FEI Talos F200S at an accelerating voltage of 200 kV. Initially, the thoroughly ground sample was dispersed in an ethanol solution, homogenized through ultrasonic agitation, and subsequently deposited onto a carbon film-coated copper mesh using a pipette. Following the drying process at ambient temperature, specimens for TEM were subsequently prepared. Additionally, annular dark field scanning transmission electron microscopy (AC-HAADF-STEM) utilizing double spherical aberration correctors and electron energy loss spectroscopy (EELS) was carried out at 200 kV. Fourier transform infrared spectroscopy (FTIR) analyses were performed utilizing the Thermo Fisher-Nicolet 6700 instrument. The FTIR spectrum was obtained using a Bruker V70 spectrometer. The N_2 adsorption and desorption isotherm (collected from Quantachrone Autosorb iQ-MP-C) was obtained to derive the surface areas and the pore size distribution of the catalysts. ICP-OES (Thermo Fisher Scientific, IRIS Intrepid II XSP spectrometer) was used to determine the contents of Fe species in the samples.

Ex situ XAFS measurements

The X-ray absorption fine structure spectra data were collected at BL14W1 station in Shanghai Synchrotron Radiation Facility (SSRF, operated at 3.5 GeV with a maximum current of 250 mA), respectively.

The data were collected at room temperature (Fe K-edge in fluorescence excitation mode using a Lytle detector). All samples were pelletized as disks of 13 mm diameter with 1 mm thickness using graphite powder as a binder.

In situ synchrotron radiation XAFS measurements

A catalyst-modified carbon paper was used as the working electrode, graphite rod as the counter electrode, and Hg/HgO electrode as the reference electrode. A homemade electrochemical cell was used for in situ XAFS measurements. The experiments were performed at the BL14W1 station in SSRF.

Electrochemical measurements for the OER

The evaluation of the electrocatalytic OER performance of *A*-$Fe_2S_1N_5$/SNC was performed with a standard three-electrode system using an electrochemical workstation (CHI 760E) in Ar-saturated 1.0 M KOH. The electrolyte employed in this study is a 1.0 M KOH solution, maintained at a constant temperature of 25 ± 2 °C. This solution was prepared by dissolving 29.5 g of 95% pure KOH in 500 mL of deionized water, while maintaining continuous agitation to guarantee thorough dissolution. The determined practical electrolyte pH value is 13.86 ± 0.06 for a 1.0 M KOH solution. Prior to its application, the pH meter was calibrated with buffer solutions of varying pH levels, specifically potassium hydrogen phthalate solution (pH = 4.00), mixed phosphate solution (pH = 6.86), and sodium tetraborate solution (pH = 9.18). The ink was prepared using 2 mg of *A*-$Fe_2S_1N_5$/SNC, 10 µL of Nafion (5 wt%), 100 µL of ethanol, and 190 µL of deionized water to form a homogeneous catalyst ink (ultrasonicated for 2 h). The working electrode was 40 µL of ink deposited on a clean carbon cloth (area: 1 cm^2). A graphite rod (counter electrode) and Hg/HgO (reference electrode) were used to perform the electrochemical tests. The catalyst loading amount on the carbon cloth was 0.26 mg cm^{-2}. Before measurement, the electrode was activated under CV conditions (scan rate 100 mV s^{-1} for 100 cycles) until stable. Linear sweep voltammetry (LSV) curves of the catalysts were obtained at a constant scanning rate (5 mV s^{-1}) with 95% *iR* compensation. All potentials were referenced to the reversible hydrogen electrode (RHE), following the below equation: $E_{RHE} = E_{Hg/HgO} + 0.098 + 0.0591\,pH$. The solution resistance (*R*s) was evaluated using electrochemical impedance spectroscopy (EIS) across a frequency range of 100 kHz to 0.1 Hz, with an applied amplitude of 5 mV. The ECSA was evaluated by the electrochemical double-layer capacitance (C_{dl}), where the C_{dl} was obtained from the CV measurements at different scan rates (from 20 to 120 mV s^{-1}) in 1.0 M KOH. The stability of the electrode materials was obtained via the chronoamperometry method. The potentiostat software captured data at one-second intervals. All the measurements were performed once.

Electrochemical measurements for ORR

The oxygen reduction reaction measurements were performed in a three-electrode cell using an electrochemical workstation (CHI 760E) setup with a rotating disk electrode (RRDE-3A). A glassy carbon (GC: 4 mm inner diameter, 0.19625 cm^2), platinum wire, and saturated calomel electrode (SCE) were used as the working, counter, and reference electrodes, respectively. The catalyst suspension was prepared by dispersing 2 mg catalyst into 250 µL ethanol/Nafion (5 wt%) mixed solution, followed by ultrasonication for 30 min to form a homogenous ink. Afterward, 10 µL ink was dropped onto the freshly polished GC electrode and naturally dried in air for all the catalysts. The catalyst loading amount on glassy carbon is 0.4 mg cm^{-2}. Before the ORR test, the electrolyte was purged with O_2 to form the O_2-saturated 0.1 M KOH solution (pH = 12.9 ± 0.12). Cyclic voltammograms were recorded at 50 mV s^{-1} in O_2-saturated 0.1 M KOH. Linear sweep voltammetry polarization curves for ORR were obtained at a rotating rate of 1600 rpm, without *iR* compensation at 5 mV s^{-1}. All potentials were referenced to the reversible hydrogen electrode (RHE), according to the reference electrode calibration: $E_{RHE} = E_{SCE} + 0.241 + 0.0591\,pH$. Durability tests were performed by cycling between 0.6 and 1.0 V versus RHE for 30,000 cycles at room temperature.

Zinc-air battery measurements

The *A*-$Fe_2S_1N_5$/SNC ink was uniformly dispersed onto Teflon-coated carbon fiber paper with the loading of 1.0 mg cm^{-2}, then dried at 60 °C. For comparison, a Pt/C electrode with the same catalyst loading was also prepared. The polished commercial Zn foil with a thickness of 0.2 mm was used as the anode. Both electrodes were constructed into a homemade Zn–air device in 6.0 M KOH and 0.2 M zinc acetate electrolyte saturated with O_2.

AEM water electrolyzer system assembly

The AEM water electrolyzer was composed of an anion-exchange membrane, electrodes, bipolar plates, current distributors, and end plates. The anode and cathode were assembled using *A*-$Fe_2S_1N_5$/SNC and commercial Pt/C, respectively. The anion exchange membrane is Sustainion X37-50 grade RT (50 µm × 2 cm × 2 cm), provided by the Sinero fuel cell store. The active area of the MEA was 4.0 cm^2 (2 cm × 2 cm). The AEM single cell was operated at room temperature with the injection of 1.0 M KOH into the MEA. The stability of the AEM single cell was tested at a constant current density of 500 mA cm^{-2} for 250 h at room temperature.

Details of the DFT calculations

All the simulations were carried out via the spin-polarized density functional theory method executed via the Vienna Ab initio Simulation Package (VASP)[55] with a projector augmented wave pseudopotential (PAW) to handle the electron–ion interactions. The PBE is functional with the scheme of the generalized gradient approximation (GGA) was applied to treat electronic exchange–correlation interactions. DFT + U correction with an effective *U* value of 4.0 eV was adopted to depict the exchange interaction of the 3D orbitals for the Fe atom, referring to a previous report on diatomic catalysts supported on a nitrogen-doped carbon substrate[56]. To describe the interactions among the intermediates and active sites accurately, the DFT-D3 dispersed corrections proposed by Grimme et al. were involved in evaluating their adsorbed free energies[57]. Considering the practical electrochemical reaction surroundings, the solvation effect was drawn into the adsorbed free energy of intermediates via a polarized continuum model—VASPsol. The electronic kinetic cut-off with the plane wave basis set was 400 eV, and the corresponding convergence criteria of total energy and residual force per atom were less than 10^{-4} eV and 0.02 eV/Å, respectively[58]. The k-point sampling mesh in the first Brillouin zone integration was 3 × 3 × 1 for geometric optimization and 5 × 5 × 1 for static simulations[59].

A symmetric Fe_2N_6/NC model constructed by embedding two Fe atoms into nitrogen-doped graphene with a 6 × 6 × 1 supercell was selected from four possible diatomic catalysts, named Fe_2N_3-6_1, Fe_2N_3-6_2, Fe_2N_4-6, and Fe_2N_4-8, according to a previous report[60,61], as shown in Supplementary Fig. 62. Given the spin-polarized characteristic of Fe, the relative energies between the ferromagnetic (FM) and antiferromagnetic (AFM) state for each model and the formation energies were systematically investigated via the PBE functional with and without DFT + U correction, as shown in Supplementary Fig. 63. Note that some AFM states with the initial setting were converted to a ferrimagnetic state after relaxation. Their ground states are AFM states, except for the Fe_2N_3-6_2 model with the FM ground state by the pure PBE method. The formation energies were calculated via the following formula: $E_f = E_{total} - aE_C - bE_{Fe} - cE_N - dE_S$, where E_{total}, E_C, E_{Fe}, E_N, and E_S are the total energies of the *A*-$Fe_2S_1N_5$/SNC and Fe_2N_6/NC models; the chemical potentials of C, Fe, N, and S refer to graphene, the metal iron bulk, the N_2 molecule, and the S_8 molecule, respectively, corresponding to the numbers marked by the letters a, b, c, and d. The Fe_2N_3-6_2 model has the lowest

formation energy, with values of −7.85 and −11.79 eV according to the PBE functional with and without DFT + U correction. Therefore, the stable Fe_2N_3-6_2 model served as the as-fabricated Fe_2N_6/NC diatomic catalyst to investigate the following OER/ORR mechanism.

Thus, the fabricated *A*-$Fe_2S_1N_5$/SNC diatomic catalyst was constructed based on the Fe_2N_3-6_2 model considering eight kinds of $Fe_2S_1N_5$/SNC configurations in Supplementary Fig. 64, named "1–8". In the Fe_2N_3-6_2 model, the "1–3" models replace one nitrogen site using one sulfur atom with different nitrogen sites. One sulfur atom substitutes one carbon and one nitrogen site with different carbon–nitrogen sites to generate models "4–6". The "7–8" models were similar to the "4–6" configurations, with fewer nitrogen atoms. The relative energies and formation energies of the PBE functional with and without DFT + U correction are displayed in Supplementary Fig. 65. Using the DFT + U method, the AFM states were their ground states, and the opposite was true for the pure PBE method, except for model "8" with the FM ground state, which had a negligible energy difference of 0.02 eV. Model "1" has the lowest formation energy, with values of −6.01 and −10.17 eV obtained via the PBE functional with and without DFT + U correction, respectively. The bond lengths of the Fe–Fe, Fe–S, and Fe–N pairs are 2.36, 2.29, and 1.96 Å, respectively, using the DFT + U method, which matches well with the EXAFS fitting results. Therefore, model "1" acted as an *A*-$Fe_2S_1N_5$/SNC diatomic catalyst for the following OER/ORR research, unlike the Fe_2N_6/NC model.

The density of state, charge, and spin population was further calculated via the VASPKIT[62] tool to treat these postprocessing results. In the electrochemical reaction, the energy of $H^+ + e^-$ was referred to as the energy of 1/2 H_2 according to the computational hydrogen model (CHE) proposed by Nørskov et al. [63]. To accurately depict the real configuration of the active site in the electrochemical surroundings, the Pourbaix diagram was calculated via the following equation:

$$* + mH_2O \rightarrow *O_mH_n + (2m - n)(H^+ + e^-)$$

$$\Delta G(U, pH) = G*_{OmHn} + (2m - n)G_{H^+ + e^-} - G* - mG_{H2O}$$

$$= G*_{OmHn} + (2m - n)(1/2G_{H2} - eU + kBTln[cH+]) - G* - mG_{H2O}$$

$$= G*_{OmHn} + (2m - n)(1/2G_{H2} - eU - 0.059pH) - G* - mG_{H2O}$$

where G = E + ZPE + ΔH(0→298.15 K) − TS. E is the DFT energy, which is the free energy correction, and for the adsorbates, it can be calculated via the vibrational frequency based on the harmonic approximation; however, for free gas molecules, the standard free energy correction was taken from the computational chemistry database (https://cccbdb.nist.gov/)[64]. The letters m and n are the numbers of oxygen and hydrogen atoms in the adsorbate, respectively. The "*" refers to an adsorption site. The electrochemical OER and ORR mechanisms were comprehensively researched via all the possible intermediates in the proton-coupling electron-transfer (PCET) processes according to our previous work[65,66].

For the electrochemical OER process, the possible elementary steps are as follows:

$$H_2O + * \rightarrow *OH + H^+ + e^- \quad (1)$$

$$*OH \rightarrow *O + H^+ + e^- \quad (2)$$

$$*OH + H_2O + * \rightarrow 2*OH + H^+ + e^- \quad (3)$$

$$*O + H_2O + * \rightarrow *OOH + H^+ + e^- \quad (4)$$

$$2*OH + *O + *OH + H^+ + e^- \quad (5)$$

$$*O + H_2O + * \rightarrow *O + *OH + H^+ + e^- \quad (6)$$

$$*OOH \rightarrow *O_2 + H^+ + e^- \quad (7)$$

$$*O + *OH \rightarrow 2*O + H^+ + e^- \quad (8)$$

$$*O_2 \rightarrow * + O_2(g) \quad (9)$$

$$2*O \rightarrow * + O_2(g) \quad (10)$$

For the electrochemical ORR process, the possible elementary steps are as follows:

$$* + O_2 + H^+ + e^- \rightarrow *OOH \quad (11)$$

$$*OOH + H^+ + e^- \rightarrow *O + H_2O \quad (12)$$

$$*O + H^+ + e^- \rightarrow *OH \quad (13)$$

$$*OH + H^+ + e^- \rightarrow * + H_2O \quad (14)$$

For the OER process, the potential-determined step (PDS) is the primary step with the maximum reaction energy value, where G_{PDS} = max {G_i}, I = 1, 2, 3, 4. The overpotential of the OER (η_{OER}) is (G_{PDS}/e − 1.23) V. For the ORR process, the PDS is the elementary step with the maximum reaction energy value, where G_{PDS} = max {G_i}, i = 1, 2, 3, 4. $\eta_{OER} = [1.23 - (-G_{PDS}/e)]/e = 1.23 + G_{PDS}/e$.

Data availability

All data supporting the findings of this study are available within the paper and its supplementary information files or from the corresponding authors upon request. Source data are provided with this paper.

References

1. Chu, S. & Majumdar, A. Opportunities and challenges for a sustainable energy future. *Nature* **488**, 294–303 (2012).
2. Armand, M. & Tarascon, J. M. Building better batteries. *Nature* **451**, 652–657 (2008).
3. Seh, Z. W. et al. Combining theory and experiment in electrocatalysis: insights into materials design. *Science* **355**, eaad4998 (2017).
4. Chang, J. et al. Improving Pd-N-C fuel cell electrocatalysts through fluorination-driven rearrangements of local coordination environment. *Nat. Energy* **6**, 1144–1153 (2021).
5. Jiao, L. et al. Chemical vapour deposition of Fe–N–C oxygen reduction catalysts with full utilization of dense Fe–N_4 sites. *Nat. Mater.* **20**, 1385–1391 (2021).
6. Li, Z. et al. Engineering the electronic structure of single-atom iron sites with boosted oxygen bifunctional activity for zinc–air batteries. *Adv. Mater.* **35**, 2209644 (2022).
7. Hou, Y. et al. Atomically dispersed nickel–nitrogen–sulfur species anchored on porous carbon nanosheets for efficient water oxidation. *Nat. Commun.* **10**, 1392 (2019).
8. Sun, L. et al. Intramolecular hydroxyl nucleophilic attack pathway by a polymeric water oxidation catalyst with single cobalt sites. *Nat. Catal.* **5**, 414–429 (2022).
9. Xu, Q. et al. Fabricating dual-atom iron catalysts for efficient oxygen evolution reaction: a heteroatom modulator approach. *Angew. Chem. Int. Ed.* **59**, 2–11 (2020).

10. Zhong, D. et al. Dinuclear metal synergistic catalysis for energy conversion. *Chem. Soc. Rev.* **52**, 3170–3214 (2023).
11. Lei, L. et al. From synthesis to mechanisms: in-depth exploration of the dual-atom catalytic mechanisms toward oxygen electrocatalysis. *Adv. Mater.* **36**, 2311434 (2024).
12. Chen, Z. et al. Thermal migration towards constructing W-W dual-sites for boosted alkaline hydrogen evolution reaction. *Nat. Commun.* **13**, 763 (2022).
13. Biswas, Sudip et al. Synergistic Al-Al dual-atomic site for efficient artificial nitrogen fixation. *Angew. Chem. Int. Ed.* **63**, e202405493 (2024).
14. Zhang, H.-T. et al. Iron-catalyzed water oxidation: O–O bond formation via intramolecular oxo–oxo interaction. *Angew. Chem. Int. Ed.* **60**, 12467–12474 (2021).
15. Wang, D. et al. Iron-catalyzed water oxidation: O–O bond formation via intramolecular oxo–oxo interaction. *Proc. Natl Acad. Sci. USA* **121**, e2317247121 (2024).
16. Meyer, T. J. et al. Electrocatalytic water oxidation by a monomeric amidate-ligated Fe(III)–aqua complex. *J. Am. Chem. Soc.* **136**, 5531–5534 (2014).
17. Costas, M. et al. Design of iron coordination complexes as highly active homogenous water oxidation catalysts by deuteration of oxidation-sensitive sites. *J. Am. Chem. Soc.* **141**, 323–333 (2019).
18. Najafpour, M. M. et al. A dinuclear iron complex with a single oxo bridge as an efficient water-oxidizing catalyst in the presence of cerium (IV) ammonium nitrate: new findings and current controversies. *Catal. Sci. Technol.* **4**, 30 (2014).
19. Müllen, K. et al. Boosting oxygen electrocatalytic activity of Fe-N-C catalysts by phosphorus incorporation. *J. Am. Chem. Soc.* **145**, 3647–3655 (2023).
20. Zhang, Z. et al. The simplest construction of single-site catalysts by the synergism of micropore trapping and nitrogen anchoring. *Nat. Commun.* **10**, 1657 (2019).
21. Chang, J. et al. A C-S-C linkage-triggered ultrahigh nitrogen-doped carbon and the identification of active site in triiodide reduction. *Angew. Chem. Int. Ed.* **60**, 3587–3595 (2021).
22. Wang, L. et al. A sulfur-tethering synthesis strategy toward high-loading atomically dispersed noble metal catalysts. *Sci. Adv.* **5**, eaax6322 (2019).
23. Mehmood, A. et al. High loading of single atomic iron sites in Fe–NC oxygen reduction catalysts for proton exchange membrane fuel cells. *Nat. Catal.* **5**, 311–323 (2022).
24. Hai, X. et al. Scalable two-step annealing method for preparing ultra-high-density single-atom catalyst libraries. *Nat. Nanotechnol.* **17**, 174–181 (2022).
25. Zeng, Y. et al. Tuning the thermal activation atmosphere breaks the activity–stability trade-off of Fe–N–C oxygen reduction fuel cell catalysts. *Nat. Catal.* **6**, 1215–1227 (2023).
26. Liu, M. et al. Ferredoxin-inspired design of S-synergized Fe–Fe dual-metal center catalysts for enhanced electrocatalytic oxygen reduction reaction. *Adv. Mater.* **36**, 2309231 (2024).
27. Shang, H. et al. Engineering unsymmetrically coordinated Cu-S_1N_3 single atom sites with enhanced oxygen reduction activity. *Nat. Commun.* **11**, 3049 (2020).
28. Shang, H. et al. Atomic design of carbon-based dual-metal site catalysts for energy applications. *Nano Res.* **16**, 6477–6506 (2023).
29. Zheng, X. et al. Theory-driven design of high-valence metal sites for water oxidation confirmed using in situ soft X-ray absorption. *Nat. Chem.* **10**, 149–154 (2018).
30. Noh, W. Y. et al. Molecularly engineered carbon platform to anchor edge-hosted single-atomic M–N/C (M = Fe, Co, Ni, Cu) electrocatalysts of outstanding durability. *ACS Catal* **12**, 7994–8006 (2022).
31. Zhang, Q. et al. S edge/center-selectively doped graphene oxide for bisphenol A electro-degradation: Preparation, efficiency and mechanism. *Chem. Eng. J.* **420**, 127669 (2021).
32. Zhang, L. et al. Highly active and durable nitrogen-doped CoP/CeO_2 nanowire heterostructures for overall water splitting. *Chem. Eng. J.* **460**, 141119 (2023).
33. Choi, H. W. et al. Trifunctional robust electrocatalysts based on 3D Fe/N-doped carbon nanocubes encapsulating Co_4N nanoparticles for efficient battery-powered water electrolyzers. *Carbon Energy* **6**, 505 (2024).
34. Magnier, L. et al. Fe–Ni-based alloys as highly active and low-cost oxygen evolution reaction catalyst in alkaline media. *Nat. Mater.* **23**, 252–261 (2024).
35. Lee, Y. J. & Park, S.-K. Synergistically coupling of Ni–Fe LDH arrays with hollow Co–Mo sulfide nanotriangles for highly efficient overall water splitting. *Rare Metals* **43**, 522–532 (2024).
36. Wang, L. et al. Asymmetric coordination of iridium single-atom IrN_3O boosting formic acid oxidation catalysis. *Angew. Chem. Int. Ed.* **62**, e202301711 (2023).
37. Jeong, Y. et al. Laser-driven liquid assembly: metal-nanocluster-decorated $Ni(OH)_2$/nickel foam for efficient water electrolysis. *SmartMat* **n/a**, e1281 (2024).
38. Oener, S. Z., Bergmann, A. & Cuenya, B. R. Designing active oxides for a durable oxygen evolution reaction. *Nat. Synth.* **2**, 817–827 (2023).
39. Wang, X. et al. Electronic structure regulation of the Fe-based single-atom catalysts for oxygen electrocatalysis. *Nano Energy* **121**, 109268 (2024).
40. Zhao, S. et al. Ultrathin metal–organic framework nanosheets for electrocatalytic oxygen evolution. *Nat. Energy* **1**, 16184 (2016).
41. Xiao, Z. et al. Operando identification of the dynamic behavior of oxygen vacancy-rich Co_3O_4 for oxygen evolution reaction. *J. Am. Chem. Soc.* **142**, 12087–12095 (2020).
42. Lu, S.-Y. et al. Synthetic tuning stabilizes a high-valence Ru single site for efficient electrolysis. *Nat. Synth.* **3**, 576–585 (2024).
43. Bai, L. et al. A cobalt–iron double-atom catalyst for the oxygen evolution reaction. *J. Am. Chem. Soc.* **141**, 14190–14199 (2019).
44. Cao, L. et al. Dynamic oxygen adsorption on single-atomic ruthenium catalyst with high performance for acidic oxygen evolution reaction. *Nat. Commun.* **10**, 4849 (2019).
45. Wang, N. et al. Doping shortens the metal/metal distance and promotes OH coverage in non-noble acidic oxygen evolution reaction catalysts. *J. Am. Chem. Soc.* **145**, 7829–7836 (2023).
46. Shi, Q. et al. Robust noble metal-based electrocatalysts for oxygen evolution reaction. *Chem. Soc. Rev.* **48**, 3181–3192 (2019).
47. Pei, Z. et al. Electrocatalytic acidic oxygen evolution: from catalyst design to industrial applications. *Matter* **6**, 4128–4144 (2023).
48. Li, R. et al. Superiority of dual-atom catalysts in electrocatalysis: one step further than single-atom catalysts. *Adv. Energy Mater.* **12**, 2103564 (2022).
49. Fang, W. et al. Durable CO_2 conversion in the proton-exchange membrane system. *Nature* **626**, 86–91 (2024).
50. Barlocco, I. et al. Does the oxygen evolution reaction follow the classical OH*, O*, OOH* path on single atom catalysts? *J. Catal.* **417**, 351–359 (2023).
51. Gono, P. et al. Effect of the solvent on the oxygen evolution reaction at the TiO_2–water interface. *J. Phys. Chem. C* **123**, 18467–18474 (2019).
52. Kumar, P. et al. High-density cobalt single-atom catalysts for enhanced oxygen evolution reaction. *J. Am. Chem. Soc.* **145**, 8052–8063 (2023).
53. Liu, F. et al. Fe/Co dual metal catalysts modulated by S-ligands for efficient acidic oxygen reduction in PEMFC. *Sci. Adv.* **9**, eadg0366 (2023).
54. Shi, Z. et al. Confined Ir single sites with triggered lattice oxygen redox: toward boosted and sustained water oxidation catalysis. *Joule* **5**, 2164–2176 (2021).
55. Sun, Z. et al. Rational construction of a triple-phase reaction zone using CuO-based heterostructure nanoarrays for enhanced water oxidation reaction. *Inorg. Chem.* **62**, 21461–21469 (2023).

56. Zhang, Y.-X. et al. General synthesis of a diatomic catalyst library via a macrocyclic precursor-mediated approach. *J. Am. Chem. Soc.* **145**, 4819–4827 (2023).
57. Ye, L. et al. A rechargeable calcium–oxygen battery that operates at room temperature. *Nature* **626**, 313–318 (2024).
58. Shi, Z. et al. Phase-dependent growth of Pt on MoS_2 for highly efficient H_2 evolution. *Nature* **621**, 300–305 (2023).
59. Zhang, L. et al. Interfacial engineering of 3D hollow $CoSe_2$@ultrathin $MoSe_2$ core@shell heterostructure for efficient pH-universal hydrogen evolution reaction. *Nano Res.* **15**, 2895–2904 (2022).
60. Zhao, T. et al. Homonuclear dual-atom catalysts embedded on N-doped graphene for highly efficient nitrate reduction to ammonia: from theoretical prediction to experimental validation. *Appl. Catal. B Environ.* **339**, 123156 (2023).
61. Han, B. & Li, F. Regulating the electrocatalytic performance for nitrogen reduction reaction by tuning the N contents in Fe_3@N_xC_{20-x} (x = 0~4): a DFT exploration. *J. Mater. Inf.* **3**, 24 (2023).
62. Wang, V. et al. VASPKIT: a user-friendly interface facilitating high-throughput computing and analysis using VASP code. *Comput. Phys. Commun.* **267**, 108033 (2021).
63. Wang, X. et al. Asymmetric Co-N_3P_1 trifunctional catalyst with tailored electronic structures enabling boosted activities and corrosion resistance in an uninterrupted seawater splitting system. *Adv. Mater.* **34**, 2204021 (2022).
64. Jia, H. et al. Unveiling the electrolyte cations dependent kinetics on CoOOH-catalyzed oxygen evolution reaction. *Angew. Chem. Int. Ed.* **62**, e202313886 (2023).
65. Dai, Y. et al. Manipulating local coordination of copper single atom catalyst enables efficient CO_2-to-CH_4 conversion. *Nat. Commun.* **14**, 3382 (2023).
66. Patel, A. M. et al. Theoretical approaches to describing the oxygen reduction reaction activity of single-atom catalysts. *J. Phys. Chem. C* **122**, 29307–29318 (2018).

Acknowledgements

This work was supported by the National Natural Science Foundation of China (Grants No. U22A20143 to B.Z., 22201262 to H.S., and 22375019 to W.C.), the Key Research & Development Project of Henan Province (241111232200 to J.W.), the Beijing Institute of Technology Research Fund Program for Young Scholars (2022CX01011 to W.C.), the Start-up Foundation for Senior Talents of Jiangsu University (21JDG041 to Z.S.), and the China Postdoctoral Science Foundation (2023M731357 to Z.S.). We thank the theoretical calculations performed on the Northwest District of the Sugon National Supercomputer Center and the A6 Zone of the Beijing Super Cloud Computing Center, supported by PARATERA. The authors thank the Center for Advanced Analysis and Gene Sequencing of Zhengzhou University and the BL14W1 in the Shanghai Synchrotron Radiation Facility (SSRF) for help with characterization.

Author contributions

L.Z., N.Z., H.S., J.W., W.C., and B.Z. conceived the idea, designed the study and wrote the paper. H.S., L.Z., and N.Z. performed the sample synthesis, performed most of the reactions, collected and analysed the data, and wrote the paper. W.C., Z.W., and Z.S. carried out the X-ray absorption fine structure characterizations and data analysis. L.Z., Y.L., and X.W. conducted the electrochemical measurements. Z.S. and H.S. performed the DFT calculations. F.Z. helped with the spherical aberration electron microscopy test and discussion. D.W., Y.Z., X.X., and B.Z. helped to check and revise the paper.

Competing interests

The authors declare no competing interests.

Additional information

Supplementary information The online version contains supplementary material available at https://doi.org/10.1038/s41467-024-53871-5.

Correspondence and requests for materials should be addressed to Huishan Shang, Jingtao Wang, Zhongti Sun or Wenxing Chen.

Peer review information *Nature Communications* thanks Jingxiang Zhao, and the other, anonymous, reviewer(s) for their contribution to the peer review of this work. A peer review file is available.